Journal Pre-proofs

Defective Titanium Dioxide Nanobamboo Arrays Architecture for Photocatalytic Nitrogen Fixation up to 780 nm

Yuanzheng Zhang, Xiang Chen, Siyao Zhang, Lifeng Yin, Yang Yang

PII: S1385-8947(20)32161-6
DOI: https://doi.org/10.1016/j.cej.2020.126033
Reference: CEJ 126033

To appear in: *Chemical Engineering Journal*

Received Date: 12 May 2020
Revised Date: 19 June 2020
Accepted Date: 21 June 2020

Please cite this article as: Y. Zhang, X. Chen, S. Zhang, L. Yin, Y. Yang, Defective Titanium Dioxide Nanobamboo Arrays Architecture for Photocatalytic Nitrogen Fixation up to 780 nm, *Chemical Engineering Journal* (2020), doi: https://doi.org/10.1016/j.cej.2020.126033

Defective Titanium Dioxide Nanobamboo Arrays Architecture for Photocatalytic Nitrogen Fixation up to 780 nm

Yuanzheng Zhang,[a] *Xiang Chen,*[a] *Siyao Zhang,*[a] *Lifeng Yin,**[ab] *Yang Yang**[c]

a State Key Laboratory of Water Environment Simulation, School of Environment, Beijing Normal University, Beijing, 100875, China;

b Linde-Robinson Laboratory, California Institute of Technology, Pasadena, California, CA 91125, USA;

c Civil and Environmental Engineering, Clarkson University, New York, CA 13699, USA.

∗ Corresponding authors.

E-mail addresses: lfyin@bnu.edu.cn (L. Yin), yanyang@clarkson.edu (Y. Yang)

Abstract

Solar-driven nitrogen fixation is a potential solution to satisfying industrial and agricultural demand, but is severely hampered by the difficulties in capturing, activating and cleaving the dinitrogen (N_2). Here, the defect TiO_2 nanobamboo arrays ($DTiO_2$ NBAs) is designed with an electro-reduction strategy, which, for the first time, successfully converted N_2 to ammonia (NH_3) in the visible and near infrared light range under ambient conditions, without any sacrificial agent or noble-metal co-catalysts. A highly selective NH_3 yield of 48.3 mg m^{-2} h^{-1} (178 μmol g^{-1} h^{-1}, no N_2H_4 formation) is obtained on the $DTiO_2$ NBAs haired titanium foil. The apparent quantum efficiency (AQE) was measured to be 0.39% at 365 nm, 0.12% at 405 nm, 0.11% at 450 nm, 0.15% at 532 nm, 0.24% at 650 nm, and 0.07% at 780 nm. It is found that the electro-reduction process creates amorphous surface layer with modest oxygen vacancy (O_{vac}) density so as to greatly enhance light harvesting, charge carrier, photo-thermal effect, as well as nitrogen adsorption and hydrogenation activity. The alternating photo-fixation pathway is also confirmed by density functional theory (DFT) calculations. This novel nanobamboo TiO_x architecture shows a potential as a new artificial nitrogen fixation for environmentally friendly NH_3 production.

Keywords: Defect TiO_2, nanobamboo, nitrogen fixation, photocatalysis, near infrared light

1. Introduction

Ammonia (NH_3) is one of the most important raw material for the fertilizer industry and basic organic chemicals [1,2]. Also, NH_3 has been long considered as an ideal hydrogen carrier owing to its high hydrogen storage density (17.6 wt %), liquefiable (<8 bar) and carbon-free features [3]. From 1908, most of the NH_3 is synthesized via the Haber-Bosch process under extremely high-pressure (>200 bar) and high-temperature (>673 K), annually consuming more than 1% of the global energy supply,and resulting in large amount of CO_2 emission [4–

6]. Thus, there is a longstanding demand for developing a renewable and scalable approach toward the cheap conversion from dinitrogen (N_2) into NH_3.

Photocatalysis can use solar energy to generate energetic electrons for N_2 activation, and provide an opportunity for the conversion from N_2 (typically water is involved) into NH_3 under ambient conditions (equation 1–2) [7–9]. The huge free energy gain ($\Delta G°$=339 kJ mol^{-1}) makes this reaction a potential new artificial photosynthesis of NH_3 (equation 3).

$$2H_2O + 4h^+ \rightarrow O_2 + 4H^+ \quad (1)$$

$$N_2 + 6H^+ + 6e^- \rightarrow 2NH_3 \quad (2)$$

$$1/2N_2 + 3/2H_2O \rightarrow NH_3 + 3/4O_2\ (\Delta G° = 339\ kJ\ mol^{-1}) \quad (3)$$

However, photocatalytic N_2 fixation is severely challenged by the low conversion efficiency from N_2 to NH_3, due to the strong N≡N triple bonds (941.69 kJ mol^{-1}) and the weak binding between N_2 and photocatalyst, which lead to a high energy barrier concerned with N_2 reduction reaction (NRR) [10,11]. Therefore, it is significantly necessary to enhance the adsorption of N_2 on the surface of photocatalyst, as well as the sufficient activation of N≡N triple bonds. To address this, one strategy is to combine nitrogenase with synthesize biomimetic photocatalysts to capture N_2 and cleave the N≡N triple bonds (equation 4) [9,12,13].

$$N_2 + 6H^+ + n\text{Mg-ATP} + 6e^- \rightarrow 2NH_3 + n\text{Mg-ADP} + n\text{Pi} \quad (4)$$

Unfortunately, the nitrogenases are easy to loss their activities in less than 45 s without the protection of microbial respiration in the real world. Alternatively, much attention has been focused on introducing defects into the crystal lattices of semiconductor photocatalysts to form unsaturated sites and surface oxygen vacancies (O_{vac}), which play an important role in enhancement of the N_2 adsorption and activitation of N≡N triple bonds [14–17]. Nevertheless, few defect-engineered photocatalysts showed satisfied NRR activity and selectivity due to improper defect concentration, weak visible-light absorption or poor anti-photocorrosion

capacity [15,18]. In this context, there is intense interest in new nanostructured catalysts that simultaneously have high activity, hight selectivity, long-term stablility and low cost [19].

Titanium dioxide (TiO_2) has long been considered as the most promising photocatalyst for scale-up applications in energy conversion, in terms of its stability, low cost and nontoxicity [20]. As early as 1977, Guth and Schrauzer reported for the first time that TiO_2 powder can reduce N_2 into NH_3 under the irradiation of ultraviolet (UV) light [21]. Recently, Hirakawa found the rutile TiO_2 (commercial name JRC-TIO-6) which was reduced under H_2 at 673 K can successfully produce NH_3 (3.81 μmol g^{-1} h^{-1}) under the UV light irradiation, which is more efficient than other commercial TiO_2 nanoparticle (P25, 3.04 μmol g^{-1} h^{-1}) for NRR [15]. However, The hydro-reduction process still be too dangerous to control. More important, JRC-TIO-6 is also an UV-driven photocatalyst (280–420 nm) which can hardly to harvest sunlight. Hence, the development of highly efficient TiO_2 photocatalysts with N_2 fixation ability under visible and near-infrared light is an ultimate goal for practical application.

Enlighted by the report that TiO_2 with O_{vac} can be excited by the visible light [22,23], we attamped to employ the defective TiO_2 ($DTiO_2$) nano-architecture to capture N_2 and conduct NRR under visible light irradiation. Compared with TiO_2 powders or membranes, the $DTiO_2$ nanotube arrays (NTAs) have the following unique advantages: (1) Their highly ordered, vertically aligned tubular structures enhance the visible light harvesting through optical scattering [24–26]. (2) $DTiO_2$ NTAs inherently have large specific surface area and tube geometry structure, which covered with high concentration of unsaturated Ti^{3+} sites along the tube wall through defect engineering, creating abundant active centers for the adsorption of N_2 [27–29]. (3) $DTiO_2$ NTAs are good for an efficient charge-carrier separation: the diffusion distance of photogenerated electron from TiO_2 nanotubes is much longer than that from powders or membranes, which lowers the surface recombination between electrons and holes [30,31].

In this work we developed a "bamboos" like $DTiO_2$ nanotube arrays by an electrochemical reduction method. The NTAs get the nanobamboo array (NBA) geometry and behave as a highly selective and stable photocatalyst toward visible light driven conversion from N_2 to NH_3 under ambient conditions. We attempted to demonstrate activatation process of the adsorbed N_2 on the surface of localized Ti^{3+} centers by the localized electrons [32]. Besides, we were concern with how the reduction process inserts the defect levels in the band gap, below the conduction band (CB) that can not only extend the optical absorption range, but also improve the separation efficiency of carriers. In addition, we tried to proof the $DTiO_2$ NBAs also benefit from the local photo-thermal effect arising from their high concentration n-type carriers. Furthermore, a detailed reaction mechanism for the N_2 photo-fixation is analyzed based on the density functional theory (DFT) simulation.

2. Experimental Section

2.1. Synthesis of $ATiO_2$ NBAs.

The titanium foils (99.9 % purity) with a thickness of 0.1 mm were used as substrates for TiO_2 nano-architecture growth, which were cleaned by ultrasonication in acetone, ethanol, and followed by rinsing with deionized (DI) water. The anodization experiment was carried out in an electrochemical reaction cell at a pulse potential (duty ratio 0.1) of 40 V for 4 h with 20 mm separation distance between the anode (titanium foils) and cathode (platinum sheet). The electrolyte was consisted of NH_4F (0.3 wt%), ethylene glycol (95 vol%) and DI water (5 vol%). After anodization, the sample was rinsed with ethanol and DI water with low ultrasonic power successively, and then dried in argon. To obtain anatase crystals TiO_2 nanobamboo arrays ($ATiO_2$ NBAs), the as-anodized sample was further annealed in a muffle furnace at 450 °C for 2 h with a heating rate of 4 °C min^{-1}.

2.2. Synthesis of $DTiO_2$ NBAs.

The $DTiO_2$ NBAs were synthesized by the electrochemical reduction of $ATiO_2$ NBAs in a two-electrode cell (platinum sheet as counter electrode and the sample as work cathode) at room temperature [33]. The electrolyte was consisted of 200 mL of ethylene glycol and 10 mL of aqueous solution with 1 mol L^{-1} of Na_2SO_4. A cathodic voltage of 6 V was then applied to the samples for 30 s. After electrochemical reduction, the samples were rinsed with DI water and dried with flowing argon. The oxygen vacancies (O_{vac}) on the surface of TiO_2 nanobamboo are easily annihilated by adsorbed oxygen [34,35]. In order to tune the defects concentration of the samples, the electrochemical reduction process was repeated three times.

2.3 Photocatalytic Nitrogen Fixation Experiments.

The nitrogen fixation experiments were performed in a 150 mL stainless steel photo-reactor covered with quartz glass (4.6 cm in diameter) at ambient pressure. Typically, the TiO_2 nanotubes film with size of 4×4 cm^2 was placed in the bottom of the reactor and 70 mL ultra-pure water added. Before irradiation, the suspension was exhausted for 10 minutes with a vacuum pump to remove dissolved air and purged with high-purity N_2 at a flow rate of 100 mL/min for 60 min to obtain a N_2-saturated aqueous suspension. The ammonia synthesis process was irradiated afterward with a 300 W Xe lamp and continually purged with high-purity N_2 at a flow rate of 3 mL/min. The reaction solution (5 mL) was intermittently collected, and the concentration of NH_4^+ in the aliquot was determined using Nessler's reagent as a chromogenic agent at 420 nm by HACH DR6000 ultraviolet spectrophotometer and ion chromatography (Dionex ICS 2100, Thermo Fisher Scientific). In order to detect the hydrogen evolution during nitrogen fixation, the photo-reactor (150 mL) was sealed with a silica gel gasket. During the irradiation, 50 μL gas was taken from the reactor at certain intervals. The quantitative analysis of H_2 is carried out by gas chromatography (GC 7890A, Agilent) with a thermal conductivity detector (TCD) according to the established hydrogen

standard curve (Fig. S1). The catalytic reaction temperatures were maintained at 25 °C by a precise thermostat.

The apparent quantum efficiency (AQE) was calculated based on the nitrogen fixation experiment under the same conditions, except that under different monochromatic LED lamp with wavelengths (365 nm, 405 nm, 450 nm, 532nm, 650nm and 780 nm) irradiation, and the NH_4^+ yields were measured after 1 h photoreaction. The values of light intensities were measured to 151, 150, 182, 150, 100 and 200 mW/cm^2, corresponding to the 365, 405, 450, 532, 650 nm and 780 nm incident wavelength with a bandwidth of ± 5 nm, respectively. The NH_4^+ yields were measured after 1 h photoreaction, and the AQE was calculated on the basis of the following equation [36]:

$$AQE = N_e/N_p = 6N_{AM}/N_p = 6nN_A h\nu/Wat \quad (5)$$

where Ne, Np and N_{AM} represent the number of reacted electrons, incident photons and generated ammonia, respectively; n represents the molar number of generated ammonia; ν, W, A and t are the incident light frequency, intensity, irradiation area and time, respectively; N_A and *h* are the Avogadro's constant and Planck constant, respectively.

2.4 Hydrazine Detection.

The amount of hydrazine was measured by the method of Watt and Chrisp [37]. Typically, 5 mL of the reaction solution was taken out and then mixed with 5 mL of the coloring solution (a mixture of 5.99 g para-(dimethylamino) benzaldehyde, 30 mL concentrated HCl and 300 mL ethanol). After 10 min, the absorbance of resulting solution was measured at a wavelength of 455 nm.

2.5. Characterization.

Field-emission scanning electron microscope (FE-SEM) was investigated through a Hitachi S-4800 at 10 kV. High resolution transmission electron microscopy (HRTEM) patterns were obtained using JEOL 2100F microscope at an acceleration voltage of 200 kV. The crystal structure of the as-synthesized products was characterized by X-ray diffraction (XRD) patterns with Cu Kα radiation at 40 kV, 40 mA. The X-ray photoelectron spectroscopy spectra (XPS) were analyzed to identify the surface chemical composition and electron structure, which was measured by an ESCSLAB 250Xi spectrometer with Al Kα-source radiation (1486.6 eV). Raman spectra were recorded on a LabRAM Raman spectrometer. A 532 nm Ar+ laser was used as excitation source. UV-vis diffuse reflectance spectra (DRS) were spectra were acquired on a SPECORD 200 ultraviolet spectrophotometer. The Brunauer-Emmett-Teller (BET) surface area of the samples were analyzed by nitrogen adsorption-desorption in a ASAP 2020. Photoluminescence spectra (PL) were obtained using a FluoroMax-4 fluorescent spectrometer at room temperature. The electron paramagnetic resonance (EPR) spectra were collected on a Bruker A300 spectrometer at 90 K. The temperature characteristics of the samples were measured by the IR thermometer (FLIR ONE). The four probe electrical resistivity and Hall Effect tests were carried out at 300 K by the Lake Shore Cryotronics on a model 8400 Hall measurement system.

2.6. Photo-electrochemistry Tests.

All measurements were performed on a PGSTAT204 electrochemical analyzer (Metrohm Autolab) with a typical three-electrode system, using the prepared samples as working electrodes, Ag/AgCl (saturated KCl) electrode as a reference electrode and a graphite rod electrode (3 mm in diameter) as the counter electrode. The light source was a 300 W Xe lamp (HSX-F 300, 350-780 nm). The photocurrent response was also measured in 0.2 M Na_2SO_4 at a bias of -0.1 V under visible light. The Mott-Schottky measurements were performed with the potentials ranging from -1.3 to 0.4 V (vs. Ag/AgCl) at the selected frequencies of 100 and

200 Hz. The electrochemical impedance spectroscopy (EIS) measurements were performed in 0.2 M Na_2SO_4 from 10^6 to 0.01 Hz with an AC amplitude of 10 mV.

2.7. Nitrogen Temperature Programmed Desorption (TPD) Measurements.

The N_2-TPD was conducted on a chemisorption instrument (Micromeritics AutoChem II 2920) with a thermal conductivity detector (TCD). Typically, 0.2 g thin film with TiO_2 nanotube samples was cut into small pieces and placed in a quartz glass tube. The samples were first pretreated for 2 h by pure He (99.999%) gas flow at 150 °C and then cooled to room temperature. Then, the N_2 adsorbed of the sample was conducted in pure (99.999%) N_2 gas flow with a flow rate of 50 ml min^{-1} for 2 h. After purging with He gas for 0.5 h to remove the residual N_2, the sample was heated to 600 °C at a rate of 10 °C min^{-1}.

2.8. In situ Fourier Transform Infrared (FTIR) Measurements.

The in situ FTIR spectra were performed by a Nicolet iS50 FT-IR spectrometer with a specially designed reaction cell at a resolution of 2 cm^{-1}. Before test, the sample was vacuum in the reaction tank at 575K for 1h. After the reaction chamber was naturally cooled to room temperature, pure Ar (99.999%) was introduced into the chamber as a protective gas to achieve atmospheric pressure. At this point, the sample spectrum should be scanned once as background value. During the in situ characterization, pure N_2 (99.999%) with H_2O vapor was continually introduced into the chamber. The spectra were collected through a MCT detector under dark condition or after a certain irradiation time using a 300 W Xe lamp.

2.9. Isotopic Labeling Experiments.

The ^{15}N isotope labeling experiments were performed to verify the origin of generating ammonia. Considering the high cost of $^{15}N_2$, this isotope test was carried out in a 150 mL closed stainless steel photo-reactor covered with quartz glass reactor. Before irradiation, the

suspension was exhausted for 60 minutes with a vacuum pump to remove dissolved air and fed with $^{15}N_2$ gas to reach 1.5 bars. The product was obtained by ^{1}H nuclear magnetic resonance (^{1}H-NMR) spectra on a Bruker Avance II 500 MHz system. The PH of the solutions was adjusted to 2 using concentrated hydrochloric acid aqueous solution. The 1 mM Maleic acid was used as the internal standard, 20% DMSO-d_6 was used in the solutions. All experiments were undertaken with water suppression and 8000 scans.

2.10. Computational Details.

All of the first-principles calculations based on density functional theory (DFT) were conducted using the Vienna ab initio simulation package (VASP) [38,39]. The ion-electron interaction was described by the projector augmented wave (PAW) method [40]. The Perdew-Burke-Ernzerhof (PBE) of generalized gradient approximation (GGA) was adopted for the electron exchange-correlation [40,41]. An energy cut-off of 400 eV for plain-wave basis sets was used. For geometry optimization, the convergence criterion for the residual force and energy on atoms was converged to less than 0.01 eV/Å and 10^{-5} eV, respectively. For the density of state (DOS) calculation, the anatase TiO_2 (101) consisting of 3×1 supercell along [010] and [10$\bar{1}$] directions were used. The system contains 72 atoms and the Brillouin zones were sampled by a Monkhorst−Pack k-point mesh with a 6×6×1 k-point grid. The vacuum thickness was set at 15 Å to avoid the interactions between adjacent slabs. Meanwhile, the same supercell with one surface oxygen vacancies was provided to simulate the oxygen-deficient TiO_2 atomic layers. The GGA + U method with the correction of the Ti 3d orbitals by U = 5.8 eV [42]. For nitrogen fixation reaction calculation, an anatase TiO_2 (101) surface model containing 72 atoms supercell was used to reduce computational demand while guaranteeing the convergence of surface energy [43]. An oxygen atom was removed on the surface to generate surface vacancy.

The Gibbs free-energies of the adsorbed state were determined as follows:

$$\Delta G = \Delta E - \Delta E_{ZPE} - T\Delta S \quad (6)$$

where ΔE is the chemisorption energy change between the reactant and product species adsorbed on catalyst surface obtained directly from DFT calculations, ΔE_{ZPE} is the change in zero-point energies, T is the temperature (298.15 K), and ΔS is the difference vibrational entropy.

3. Results and Discussion

$ATiO_2$ NBAs were prepared by anodizing titanium foils and subsequently annealing in a muffle furnace. The $DTiO_2$ NBAs were obtained by further moderate cathodic reduction in electrolyte as described in the Experimental Section. The SEM and TEM images of the $DTiO_2$ and $ATiO_2$ NBAs (Fig. 1 and Fig. S2) both show the ordered nanobamboo array structure standing vertically to the Ti substrate, with a tube diameter of ca. 100 nm and tube wall thickness of 10 nm [25]. From inset image in Fig. 1a, the "bamboo" like tubes display a clear annulated architecture, which amplifies the surface area of NBAs structure, and, to some extent, tunes the photo-thermal and photonic crystal effect. The pore structures and BET surface areas of the $DTiO_2$ NBAs were measured by N_2 adsorption–desorption measurements at 77 K. As shown in Fig. S3, the BET surface area is estimated to be 58 $m^2\ g^{-1}$ and the pore sizes mainly distributed at 90–120 nm, which is consistent with the results of Fig. 1b. The HRTEM images and related fast Fourier transform (FFT) provided detail information on the surface structure of TiO_2 crystalline phase. In both Fig. S4 and Fig. 1c, a highly crystalline structures with a lattice space of 0.35 nm were observed, which can be assigned to the (101) planes of anatase TiO_2 [44]. In addition, the inset FFT image also confirms the same anatase nanocrystal. After electro-reduction, the surface crystalline structures were observably

collapsed: An obvious disordered layer with thickness of 2–4 nm was observed on the surface of NBAs (along the yellow dashed line, Fig. 1d), while there is no appearance of disordered amorphous phase in pure $ATiO_2$ NBAs (Fig. S4), suggesting that electro-reduction treatment unambiguously reconstructed an amorphous Ti-O_x thin layer. XRD analysis was also used to reveal the crystal structural changes before and after electro-reduction treatment (Fig. S5). Both samples have the similar diffraction peaks, which can be indexed as anatase phase (JCPDF 21-2172) [45]. However, the intensity of diffraction peaks of $DTiO_2$ NBAs much lower than that of $ATiO_2$ NBAs, indicating that the electro-reduction treatment, to some extent, destroyed the long-range patterns, thus reducing the crystallinity.

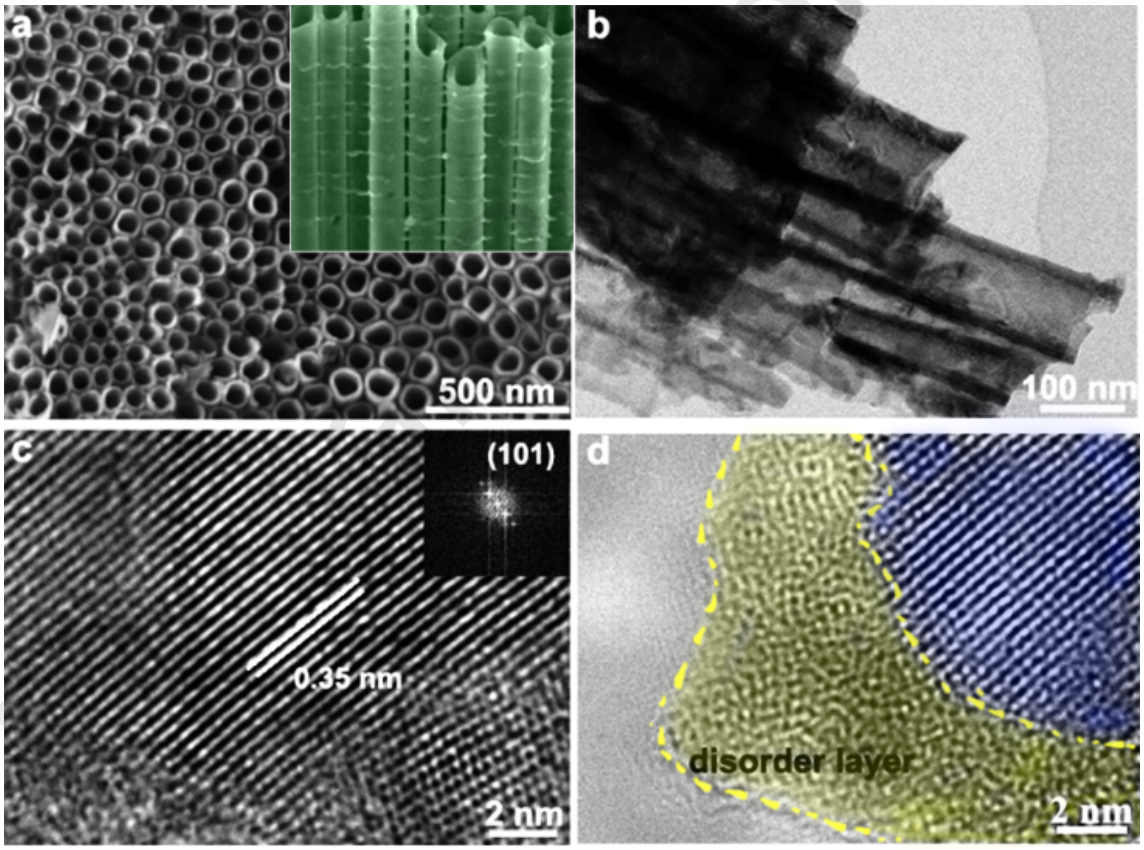

Fig. 1. a) SEM image; inset (a) the "bamboo" like vertical $DTiO_2$ NBAs. b) TEM image, and c, d) HRTEM images of $DTiO_2$ NBAs; Inset (c) the corresponding FFTs along the crystal (101) plane of the anatase TiO_2; (d) The yellow dashed line compartmentalizes the ordered crystalline anatase and the disordered amorphous TiO_x generated by electro-reduction.

Raman spectroscopy was further conducted to investigate the local structure properties. As shown in Fig. 2a, the peak intensity of $DTiO_2$ NBAs obviously decreased, which was typically characteristic of the disordered phase on the surface [46]. This is well consistent with the observation in HRTEM and XRD. Additionally, both samples have similar Raman peaks, but the slight blue-shift of Raman peak positions ranging from 100 to 800 cm^{-1} is observed on $DTiO_2$ NBAs. It could be attributed to non-stoichiometry of Ti/O on the surface of $DTiO_2$ NBAs caused by O_{vac} [47]. The XPS reveals that the Ti 2p peak of $DTiO_2$ NBAs also slightly shift to lower binding energy (Fig. S6). This may be due to the reduction process accompanied by the formation of Ti^{3+} sites associated with O_{vac}, as well as the Ti local coordination number decrease [48]. Furthermore, the colour of the NTAs changed from light grey to dark blue after reduction treatment (Fig. S7). The extended adsorption spectrum was mainly caused by the F' colour centre of anatase with high concentration of O_{vac} [49,50].

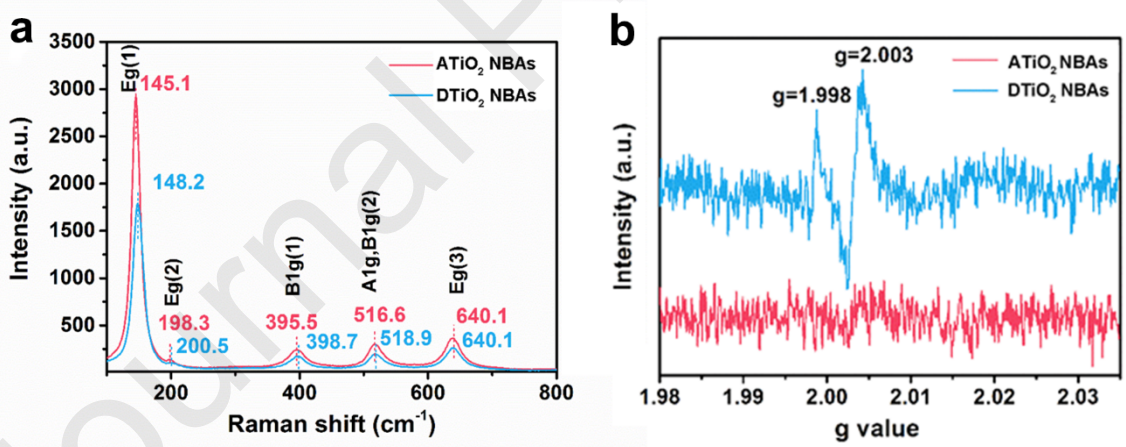

Fig. 2. a) Raman spectra of $ATiO_2$ NBAs and $DTiO_2$ NBAs. b)Low-temperature EPR patterns for $ATiO_2$ NBAs and $DTiO_2$ NBAs obtained on a Bruker A300 spectrometer at 90 K.

Low-temperature EPR was further employed to confirm the presence of defects on the surface of $DTiO_2$ NBAs (Fig. 2b). It can be observed that $ATiO_2$ NBAs is EPR silent, while the $DTiO_2$ NBAs shows distinct EPR signals at approximately g = 2.003 and g = 1.998, respectively. The signal at g = 2.003 can be attributed to the electrons localized on O_{vac} [51].

The observed signal at g = 1.998 is attributed to paramagnetic Ti^{3+} centers. This is mainly because the electrons shared by Ti-O bond can be transferred to the adjacent Ti^{4+} to produce the reduced Ti^{3+} polarons [32,52]. To understand the electronic structure of $DTiO_2$ NBAs, the ultraviolet–visible (UV-vis) absorption spectra were used to determine the optical properties of the samples, including commercial P25 (Degussa made nano-TiO_2), $ATiO_2$ NBAs and $DTiO_2$ NBAs (Fig. 3a). All samples display excellent intrinsic light absorption in the UV range. Moreover, both NTAs, no matter $ATiO_2$ or $DTiO_2$ NBAs, largely extend the light absorption to visible light, which can be attributed to the slow photon effect on the ordered $ATiO_2$ NBAs photonic crystal structure, or F' colour centre [24–26,53]. Notably, the $DTiO_2$ NBAs show an additional significant absorption in the visible–near infrared (Vis-NIR) region (Fig. 3b), which results from the polaron absorption with the Ti^{3+} as the host polarons induced by localized electrons [54–56]. This also indicates the presence of impurity levels in the $DTiO_2$ NBAs bandgap region. To further prove the result, the density functional theory (DFT) calculation was carried out to investigate the electronic band structure changes of $ATiO_2$ NBAs before and after reduction treatment (Fig. 3c and d). For the model, the anatase TiO_2 (101) slab containing six layers with and without a surface O_{vac} are adopted (Fig. S8) [43]. The density of states (DOS) reveal that the O_{vac} bring a localized electronic state composed of the Ti 3d orbital just below the CB by ~0.32 eV, indicating that the electrons present at O_{vac} sites are ionized and localized at Ti atoms to form small polarons (inset Fig. 3d) [57]. In addition, the formed shallow donor level can directly excite the local electrons to CB, thus contributing to the visible light response [58–60].

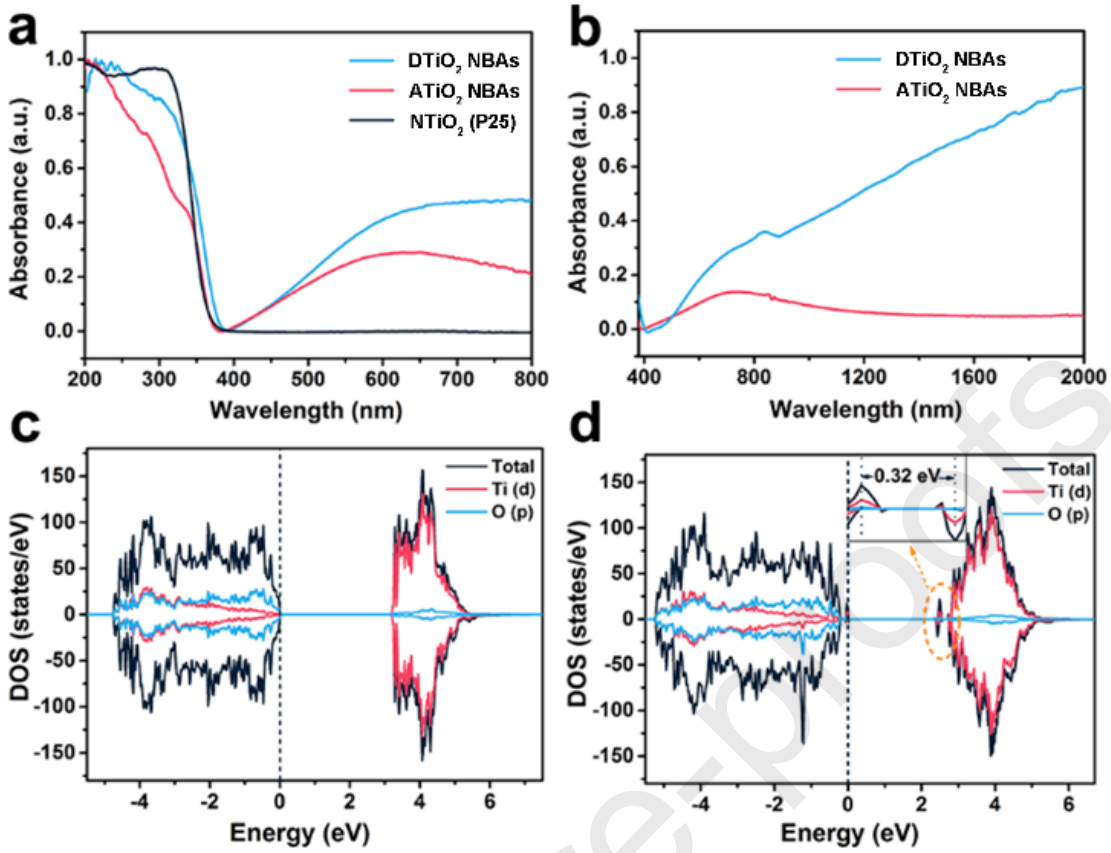

Fig. 3. a) UV-vis absorption spectra of P25, $ATiO_2$ and $DTiO_2$ NBAs. b) Vis-NIR absorption spectra ,and c, d) the calculated density of states (DOS) of $ATiO_2$ and $DTiO_2$ NBAs.

The PL, Hall measurement and photoelectrochemical analyses were further carried out to investigate the carrier characteristics in $DTiO_2$ NBAs. Fig. 4a shows the comparison of PL spectra of $ATiO_2$ NBAs and $DTiO_2$ NBAs in the wavelength range of 350–600 nm with the excitation at 325 nm at room temperature. The first peak at 400 nm (3.1 eV) was ascribed to the emission of band-gap transition. Other than that, there are 4 peaks observed in range of 440–500 nm, which can be assigned to excite photoluminescence. The peaks at 450 and 468 nm are from the band-edge free excitons, and the other two peaks at 480 and 491 nm are attributed to bound excitons [45,61]. It is clear that the PL intensity of $DTiO_2$ NBAs is much lower than that of $ATiO_2$ NBAs, indicating less recombination of the charge carriers. As shown in Fig. 4b, both samples show a fast photocurrent response to periodic light on-off. The photocurrent intensity of $DTiO_2$ NBAs is much higher than that of $ATiO_2$ NBAs, indicating

the carrier separation in $DTiO_2$ NBAs is under a better condition. This is mainly due to the coated Ti-O_x layer on the surface of $ATiO_2$, which leads to the formation of impurity levels and carrier trapping centres, thus promoting the separation of photo-generated electrons and holes, and inhibiting their recombination [62,63].

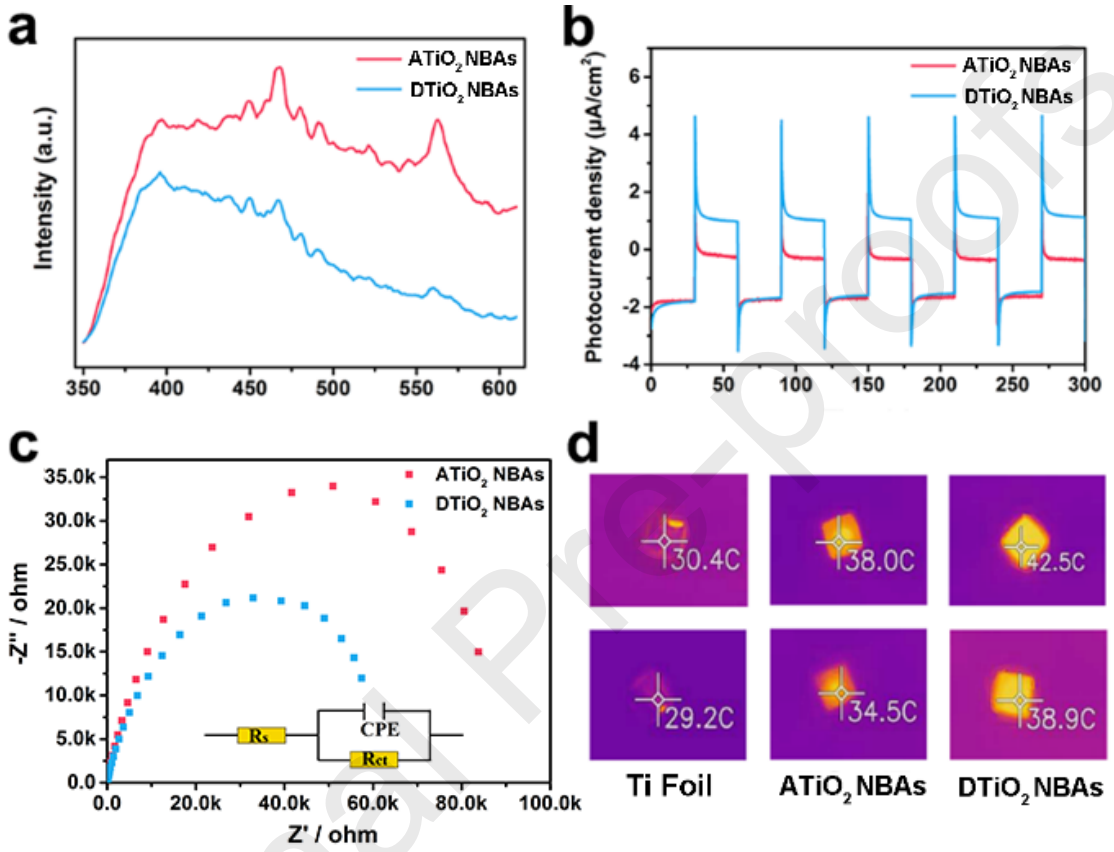

Fig. 4. a) Room-temperature PL emission spectra, b) Transient photocurrent responses, and c) EIS Nyquist plots of $ATiO_2$ and $DTiO_2$ NBAs. d) Thermographic photographs of the Ti foil, $ATiO_2$ and $DTiO_2$ NBAs. The first three were exposed to an 650 nm LED at the density of 0.1 W cm^{-2}, and the last three were exposed to an 780 nm LED at the density of 0.2 W cm^{-2}.

In addition, the EIS were carried out to investigate the charge transfer performance. The impedance spectra of $ATiO_2$ and $DTiO_2$ NBAs are both showing single semicircles (Fig. 4c), which implies that the electrode reaction is charge transfer controlled and can be modeled as an electric equivalent circuit (Fig. 4c inset) with a parallel combination of the double-layer capacitance (CPE), and the charge transfer resistance (Rct) in series with the solution

resistance (Rs). Table S1 shows the main parameters of equivalent circuit for the impedance data of the samples. It can be found that the Rct and Rs values of $DTiO_2$ NBAs is much smaller than that of $ATiO_2$ NBAs, indicating that the resistance of the carrier transfer decreased immediately. Hall Effect tests were also carried out to further reveal the effect of reduction treatment on the electronic properties of samples. Although the Ti foil substrate may affect the test data, it did not change the overall trend of sample performance. As shown in Table 1, the Hall coefficient (RH) displays that both the $ATiO_2$ NBAs and $DTiO_2$ NBAs are n-type semiconductors. The carrier concentrations (n) of $ATiO_2$ NBAs and $DTiO_2$ NBAs are 8.997×10^{12} cm^{-3} and 1.750×10^{15} cm^{-3} respectively, indicating that reduction treatment results in more Ti^{3+} species with local electronic states, thus increasing the carrier concentration. The calculated van der Pauw resistivity (ρ) of $DTiO_2$ NBAs is much lower than that of $ATiO_2$ NBAs, mainly caused by the high carrier concentration of $DTiO_2$ NBAs. However, electron carrier mobility (μ_e) of $DTiO_2$ NBAs is lower than that of $ATiO_2$ NBAs, further demonstrated that the surface lattice distortion can induce the formation of small polarons and suggest that the conduction of electrons is dominated by small polaron hopping [32,57,64]. Moreover, the concentration of free carriers or small polarons in $DTiO_2$ NBAs is significantly increased by introducing defects. The increased free carrier concentration not only enhances the NIR absorption of the semiconductor, but also improves the light to heat conversion (photo-thermal) efficiency due to a high probability of non-radiative recombination [65]. In order to confirm the photo-thermal effect, we measured the surface temperature of the sample under the irradiation of NIR light. As shown in Fig. 4d, the surface temperature of the $DTiO_2$ NBAs rapidly increased to 42.5°C and 38.9°C under the 650 and 780 nm red light irradiation, respectively. By contrast, under the identical illumination condition, the surface temperature of the $ATiO_2$ NBAs only reached 38°C and 34.5°C, respectively, indicating that the local surface photo-thermal effect on $DTiO_2$ NBAs has been enhanced due to the high probability of non-radiative relaxation occurred in the Ti3d orbital [66,67].

Table 1. AC field Hall effect data taken at 300 K.

Sample	RH[a]	n[b] (cm^{-3})	ρ[c] (Ω-cm)	μ_e [d] ($cm^2V^{-1}s^{-1}$)
TiO_2 NTAs	-693574	8.997×10^{12}	37686.4	18.399
$DTiO_2$ NBAs	-3566	1.750×10^{15}	713.3	4.998

[a] RH, Hall coefficient, [b] n, carrier concentration, [c] ρ, resistivity, and [d] μ_e, electron carrier mobility.

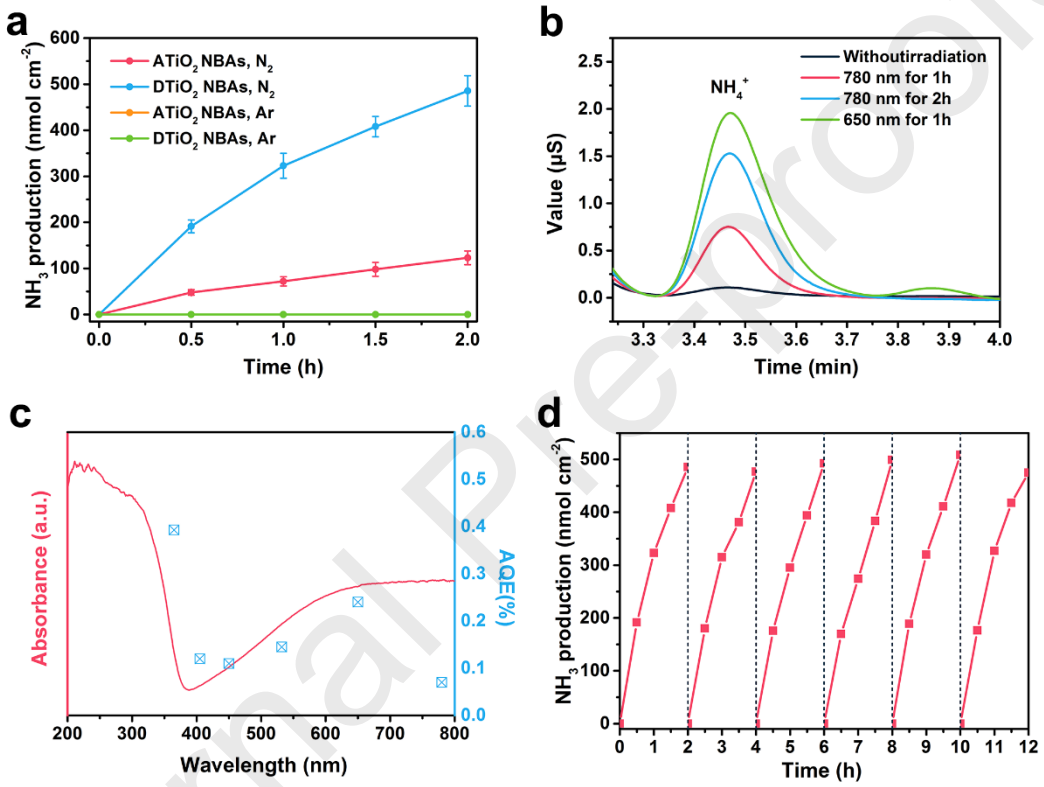

Fig. 5. a) Time course of NH_3 evolution in the photocatalytic NRR in N_2 or Ar saturated pure water under 300 W Xenon lamp irradiation. b) Peaks of NH^{4+} in Ion chromatography. The NH_4^+ generated on $DTiO_2$ NBAs under 650 nm and 780 nm monochromatic irradiation. c) The AQE of NH_3 evolution by N_2 photo-fixation for $DTiO_2$ NBAs under monochromatic lamp irradiation at different wavelengths. d) Multicycle N_2 fixation with $DTiO_2$ NBAs.

To quantify the performance of the NTAs samples for photocatalytic nitrogen fixation, the $DTiO_2$ and $ATiO_2$ NBAs films with size of 4×4 cm^2 were placed in a single compartment cell and immersed in N_2-saturated water with continuous N_2 bubbling. Both samples were

employed to produce NH_3/NH_4^+ which was detected by Nessler's reagent and ion chromatography (Fig. S9). The concentration of NH_3/NH_4^+ increased linearly with irradiation time, while no NH_3/NH_4^+ was detected in the case of purging with Ar (Fig. 5a). The NH_3/NH_4^+ evolution efficiency on $DTiO_2$ NBAs was estimated to be 284.2 nmol cm^{-2} h^{-1} (48.3 mg m^{-2} h^{-1}), corresponding to 178 μmol g^{-1} h^{-1} (0.03 g freestanding $DTiO_2$ NBAs on film) under Xenon lamp irradiation, which is almost 4 times higher than that of $ATiO_2$ NBAs (61.5 nmol cm^{-2} h^{-1}). In addition, the photocatalytic activity of the $DTiO_2$ NBAs is also significantly higher than that of the defect TiO_2 nanoparticles ($DTiO_2$ NPs), as shown in Fig. S10. Meanwhile, the NH_3/NH_4^+ yield on $DTiO_2$ NBAs under AM1.5 light irradiation was also 4.3 times higher than that of $ATiO_2$ NBAs (35.1 nmol cm^{-2} h^{-1}) (Fig. S11 and Fig. S12a). These results show that the $DTiO_2$ NBAs performed better than the previous reported photocatalytic membranes, as summarized in Table S2. We also explored the possible side reactions of N_2 fixation. The side reaction of H_2 evolution rate was estimated to be 7.4 nmol cm^{-2} h^{-1} (Fig. S12b). The produced H_2 amount was found to be only ca. 3 mol% with respect to the harvested NH_3. In addition, no apparent N_2H_4 was detected (Fig. S13 and S14), which means that the $DTiO_2$ NBAs has a high selectivity for NH_3 synthesis from N_2 reduction. A control experiment by substituting water with acetonitrile revealed no NH_3 production. Besides, the NH_3 yield in aqueous solution containing 10% methanol was much higher than that in the water system because methanol is easy to be oxidized by h^+ as a sacrificial electron donor (Fig. S15). This indicates that in the present water/N_2 system, water is the electron donor for NRR [15].

Since the $DTiO_2$ NBAs showed strong light absorption in Vis-NIR region, we executed N_2 reduction tests under monochromatic light at 650 and 780 nm. The yield of NH_3 production was detected by ion chromatography (Fig. 5b), the NH_3 yield on $DTiO_2$ NBAs was 107 nmol cm^{-2} h^{-1} at 650 nm, and 45 nmol cm^{-2} h^{-1} at 780 nm. The AQE for $DTiO_2$ NBAs under the

monochromatic light irradiation, which closely matched the absorption spectrum in the visible region (Fig. 5c). The AQE was calculated to be 0.39% at 365 nm, 0.12% at 405 nm, 0.11% at 450 nm, 0.15% at 532 nm, 0.24% at 650 nm, and 0.07% at 780 nm. Although the wavelength (450, 532, 650, and 780 nm) was far away from the cut-off absorption edge (400 nm) of $DTiO_2$ NBAs, the N_2 reduction can still be triggered, which could be attributed to the indirect excitation caused by the defect states in $DTiO_2$ NBAs [16,68]. The stability of the $DTiO_2$ NBAs catalyst for N_2 reduction was evaluated by conducting 6 successive cycles. No noticeable decrease on the NH_3 production efficiency was observed (Fig. 5d). Further, XRD patterns and XPS spectra of $DTiO_2$ NBAs evidenced no obvious change was found on the structure and surface states of $DTiO_2$ NBAs before and after the durability test (Fig. S16).

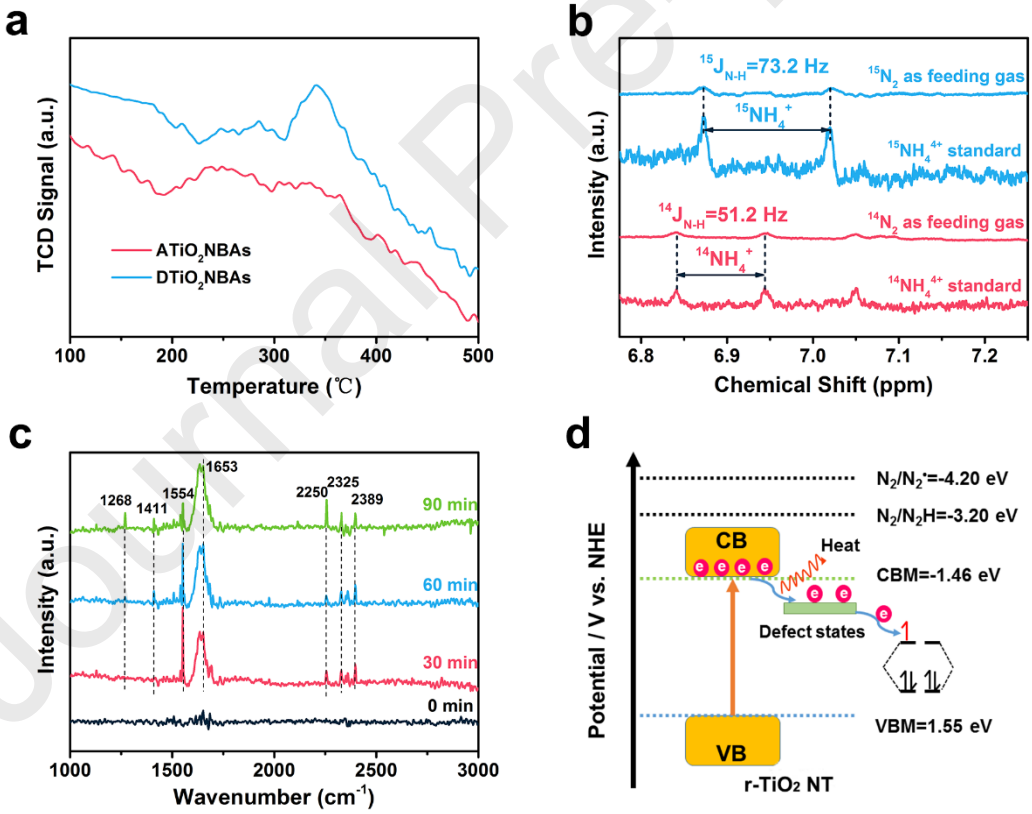

Fig. 6. a) N_2-TPD profiles of $ATiO_2$ NBAs and $DTiO_2$ NBAs. b) ^1H NMR spectra of solution after N_2 fixation reaction using $DTiO_2$ NBAs as a photocatalyst in the $^{14}N_2$ or $^{15}N_2$ atmosphere.

c) *In situ* FTIR spectra recorded from $DTiO_2$ NBAs under Xenon lamp irradiation in the presence of N_2 and water. d) Electronic energy-level diagram of $DTiO_2$ NBAs.

The N_2 absorption behaviours were performed by N_2-TPD measurements. As shown in Fig. 6a, the $DTiO_2$ NBAs exhibited a much stronger N_2 desorption peak than $ATiO_2$ NBAs in the range of the 300–370°C, which is closely related to the chemical adsorption capacity of the samples for N_2 at room temperature. This finding suggested that the O_{vac} in $DTiO_2$ NBAs provide considerable chemical adsorption sites to capture N_2 from aqueous solution. As the N_2 adsorption is the initial step for NH_3 fixation reaction, the favourable N_2 adsorption on $DTiO_2$ NBAs is beneficial for the whole NRR process [69]. To verify the origin of synthesized ammonia, an isotopic labelling study using $^{15}N_2$ as a nitrogen source was conducted [13]. As revealed by ^{1}H-NMR spectra (Fig. 6b), the ^{1}H-NMR signal of reaction solution in the $^{14}N_2$ atmosphere is split into a triplet symmetric signals with spacing of 51.2 Hz, which is consistent with the standard $^{14}NH_4^+$ solution at the same chemical shift region. A doublet signal with a spacing of 73.2 Hz was observed in the reaction solution with the $^{15}N_2$ atmosphere, which agrees well with the signal of standard $^{15}NH_4^+$ solution [70,71]. These results confirmed that the NH_3 was indeed originates from N_2.

To probe the photocatalytic NRR process, *in situ* FTIR spectra ware applied to identify reaction intermediates on the surface of $DTiO_2$ NBAs under the NRR condition (Fig. 6c). Several absorption bands gradually arise with the irradiation. Specifically, the peaks at 2250, 2325 and 2389 cm^{-1} are characteristic for the chemisorbed N_2 species [72,73]. The peak location at 1653 cm^{-1} can be assigned to ν(OH) bending mode due to the adsorbed water [74]. The peak at 1268 cm^{-1} can be attributed to the wagging mode of $-NH_2$ [36]. The band at 1554 cm^{-1} is in good agreement with the σ(N-H) bending mode derived from intermediates and NH_3 species [18,36]. Furthermore, the band at 1411 cm^{-1} arise from the characteristic absorption of NH_4^+ [16]. To eliminate the interference by adsorbed water on the identification

of nitrogen-containing functional groups, the in situ FTIR spectra for H_2O adsorbed on the $DTiO_2$ NBAs surface were also observed (Fig. S17). It is seen that the bands of adsorbed H_2O located at 1575-1725 and 3200-3700 cm^{-1}, which are not coincided with the bands of nitrogen-containing functional groups. The electronic structure of $DTiO_2$ NBAs was also studied by Mott-Schottky (MS) plots and XPS valence band (VB) spectra for in-depth investigate the catalytic mechanism (Fig. S18). Combined with the result of DFT calculation that the defect states are formed below the CB of the $DTiO_2$ NBAs, the electronic energy-level diagram of $DTiO_2$ NBAs was obtained (Fig. 6d). From thermodynamic point of view, the CB potential of $DTiO_2$ NBAs is too high to directly reduce N_2. However, the defect sites on $DTiO_2$ NBAs surface can chemisorb N_2, and serve as electron trap centres, which enhanced the photo-generated electrons transfer from $DTiO_2$ NBAs to the empty antibonding orbitals (π^*) of adsorbed N_2, thus promoting the N_2 activation and cleaving of N≡N triple bond [16,18].

The first principles calculations were performed to get further insight into the N_2 adsorption, activation and conversion processes on the surface of $DTiO_2$ NBAs. It is well-established that the chemisorption of N_2 on the catalyst surface is the prerequisite for efficient nitrogen fixation. As expected, the N_2 molecule could be adsorbed on the oxygen vacancy of $DTiO_2$ NBAs with a terminal end-on structure and form a bond with the sideward Ti atom (Fig. S19). Charge density difference of $DTiO_2$ NBAs with the adsorption of N_2 is further calculated (Fig. 7a). Both the electronic exchange and transfer between the two sideward Ti atoms and N_2 were observed. This results agree well with the "acceptance-donation" process between the transition metal and N_2 [75]. The Ti atom would accept lone-pair electrons and simultaneously donate available d-orbital electrons back transfer into the π N−N antibonding orbital to activate the N_2, which activates or weakens the N≡N triple bond [16,18]. It is believed that the end-on adsorbed N_2 are converted to NH_3 through the distal or alternating

mechanisms, including six consecutive protonation and reduction processes (Fig. S20) [76,77]. Therefore, we studied the conversion of the activated N_2 to NH_3 processes on the surface of $DTiO_2$ NBAs, following the two mechanisms. The optimized geometric structures of various intermediates along the reaction path of distal and alternating pathways are presented in Fig. S21 and S22. Fig. 7b summarizes the N-N bond length changes at various states of each elementary step. It turns out that the defect sites as chemical adsorption centres of N_2 indeed weaken the N_2 triple bond, increasing the N≡N distance to 1.132 Å (compared with 1.078 Å for free molecular N_2).

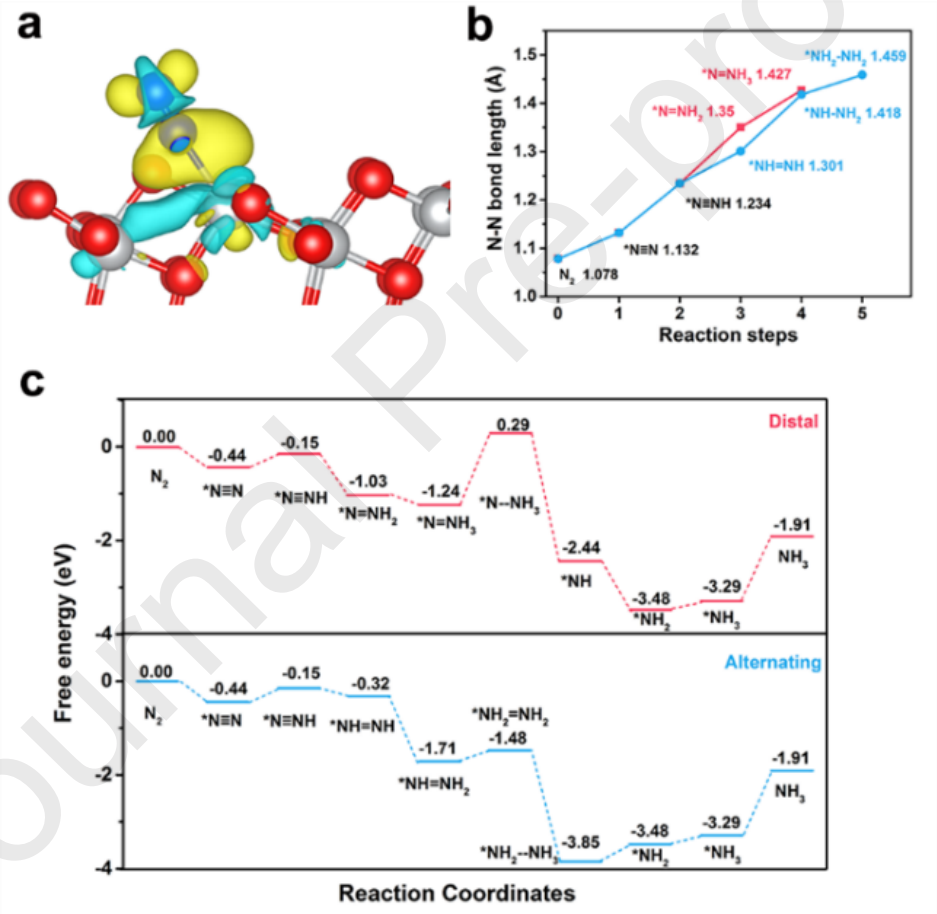

Fig. 7. a) Difference charge density of the $DTiO_2$ NBAs absorbed by N_2. The yellow and blue isosurfaces represent charge accumulation and depletion in the space, respectively. b) The N≡N bond length changes with the reaction process. c) Free energy diagrams for N_2 reduction on $DTiO_2$ NBAs through distal and alternating mechanisms.

The increasing N-N bond length of subsequent intermediates demonstrated that N≡N triple bonds could be continuously weakened until the generation of NH_3. The Gibbs free energy (G) for each step involves in the N_2 fixation was also calculated to provide a theoretical insight into the reaction mechanism (Fig. 7c). The initial adsorption of N_2 in this end-on configuration releases 0.44 eV free energy. Owing to the high binding strength between N_2 and $DTiO_2$ NBAs, the adsorbed N_2 will be hydrogenated by adsorbing a proton coupled with an electron transfer to form *N≡NH specie is very easy with the free energy uphill of 0.29 eV. For the subsequent steps through the distal pathway, the hydrogen species (H^+ + e^-) consecutively attack the distal N atoms. It can be found that there are two free energy uphill elementary reaction steps, including the first NH_3 molecule released (*N= NH_3 to *N--NH_3), the second NH_3 formation (*NH_2 to *NH_3). The Gibbs free energy changes (ΔG) for the two steps are +1.53 and +0.19 eV, respectively. Therefore, in the distal pathway, the formation of the first NH_3 molecule is the ratel-limiting step due to the maximum ΔG values (+1.53 eV) among all elementary steps. For the alternating pathway, the hydrogenation alternately occurs between the two N atoms. Different from the distal pathway, there are three free energy uphill elementary reaction steps, including *NH=NH_2 →*NH_2= NH_2 reaction, the first NH_3 released reaction (*NH_2-NH_3 to *NH_2), and the second NH_3 formation reaction (*NH_2 to *NH_3). The ΔG values for the three steps are +0.23, +0.37, and +0.19 eV, respectively. The rate-limiting step in the alternating pathway corresponds to the first NH_3 formation reaction (*NH_2-NH_3 to *NH_2) with a barrier of 0.37 eV, which is much lower than that of distal (1.53 eV) pathway, indicating that the NRR on the $DTiO_2$ NBAs surface prefers to proceed through the alternating mechanism. By contrast, the desorption of the NH_3 molecule (*NH_3 to NH_3) demands 1.38 eV free energy. However, such a process remains energetically efficient because a large amount of free energy has beeen accumulated in previous reaction steps (3.29 eV at potential of 0.00 eV) [3,77].

4. Conclusion

In summary, we found a potential candidate plucked from traditional photocatalysts for the solar-to-chemical conversion from N_2 to NH_3 on $DTiO_2$ NBAs. The reduction treatment resulted in the O_{vac} formed and created a large number localized Ti^{3+} centers, also known as small polarons, which simultaneously enhanced photon absorption, carrier density, electronic conductivity and local thermal effect, thus endowing $DTiO_2$ NBAs with excellent performance for Vis-NIR driven reduction of N_2 with an apparent quantum efficiency of 0.24% at 650 nm, and 0.07% up to 780 nm. Isotopic experiments confirmed that the synthetic NH_3 was completely derived from the supplied N_2. Moreover, experimental results and DFT calculations show that the Ti^{3+} centers of $DTiO_2$ NBAs are active sites for N_2 chemisorption and N≡N triple bond cleavage. For the subsequent N_2 reduction process, the computed onset potential is only 0.37 V through the alternating hydrogenation mechanism. We expect this strategy can be applied to develop other efficient noble-metal free defect photocatalysts for the creation of highly active N_2 reduction operating in ambient conditions.

Appendix A. Supplementary data

Supplementary data to this article can be found online at DOI: XXXX.

Acknowledgements

This work was financially supported by the National Natural Science Foundation of China (Grant 21777009), the Bill and Melinda Gates Foundation (BMGF RTTC Grants OPP1111246 and OPP1149755), Beijing Natural Science Foundation (Grant 8182031), and Major Science and Technology Program for Water Pollution Control and Treatment (Grant 2018ZX07109).

Declaration of interests

The authors declare no conflict of interest.

References

[1] R. Victor, D. Matteo, M.T. Groot, De, M.T.M. Koper, Nitrogen cycle electrocatalysis, Chem. Rev. 109 (2009) 2209.

[2] D. Sippel, M. Rohde, J. Netzer, C. Trncik, J. Gies, K. Grunau, I. Djurdjevic, L. Decamps, A. Sla, O. Einsle, A bound reaction intermediate sheds light on the mechanism of nitrogenase, Science 359 (2018) 1484-1489.

[3] W. Qiu, X.-Y. Xie, J. Qiu, W.-H. Fang, R. Liang, X. Ren, X. Ji, G. Cui, A.M. Asiri, G. Cui, B. Tang, X. Sun, High-performance artificial nitrogen fixation at ambient conditions using a metal-free electrocatalyst, Nat. Commun. 9 (2018) 3485.

[4] T. Oshikiri, K. Ueno, H. Misawa, Selective dinitrogen conversion to ammonia using water and visible light through plasmon-induced charge separation, Angew. Chem. Int. Ed. 128 (2016) 4010-4014.

[5] S. Licht, B. Cui, B. Wang, F.F. Li, J. Lau, S. Liu, Ammonia synthesis by N_2 and steam electrolysis in molten hydroxide suspensions of nanoscale Fe_2O_3, Science 45 (2015) 637-640.

[6] M. Kitano, Y. Inoue, Y. Yamazaki, F. Hayashi, S. Kanbara, S. Matsuishi, T. Yokoyama, S.W. Kim, M. Hara, H. Hosono, Ammonia synthesis using a stable electride as an electron donor and reversible hydrogen store, Nat. Chem. 4 (2012) 934-940.

[7] T. Oshikiri, K. Ueno, H. Misawa, Plasmon-induced ammonia synthesis through nitrogen photofixation with visible light irradiation, Angew. Chem. Int. Ed. 53 (2015) 9802-9805.

[8] T. Hou, Y. Xiao, P. Cui, Y. Huang, X. Tan, X. Zheng, Y. Zou, C. Liu, W. Zhu, S. Liang, L. Wang, Operando oxygen vacancies for enhanced activity and stability toward nitrogen photofixation, Adv. Energy Mater. 0 (2019) 1902319.

[9] K.A. Brown, D.F. Harris, M.B. Wilker, A. Rasmussen, N. Khadka, H. Hamby, S. Keable, G. Dukovic, J.W. Peters, L.C. Seefeldt, Light-driven dinitrogen reduction catalyzed by a CdS: nitrogenase MoFe protein biohybrid, Science 352 (2016) 448-450.

[10] J. Li, H. Li, G. Zhan, L. Zhang, Solar water splitting and nitrogen fixation with layered bismuth oxyhalides, Acc. Chem. Res. 50 (2017) 112-121.

[11] D. Zhu, L. Zhang, R.E. Ruther, R.J. Hamers, Photo-illuminated diamond as a solid-state source of solvated electrons in water for nitrogen reduction, Nat. Mater. 12 (2013) 836-841.

[12] A. Banerjee, B.D. Yuhas, E.A. Margulies, Y. Zhang, Y. Shim, M.R. Wasielewski, M.G. Kanatzidis, Photochemical nitrogen conversion to ammonia in ambient conditions with FeMoS-chalcogels, J. Am. Chem. Soc. 137 (2015) 2030-2034.

[13] J. Liu, M.S. Kelley, W. Wu, A. Banerjee, A.P. Douvalis, J. Wu, Y. Zhang, G.C. Schatz, M.G. Kanatzidis, Nitrogenase-mimic iron-containing chalcogels for photochemical reduction of dinitrogen to ammonia, P. Nati. Acad. Sci. USA. 113 (2016) 5530-5535.

[14] C. Liang, H.-Y. Niu, H. Guo, C.-G. Niu, D.-W. Huang, Y.-Y. Yang, H.-Y. Liu, B.-B. Shao, H.-P. Feng, Insight into photocatalytic nitrogen fixation on graphitic carbon nitride: Defect-dopant strategy of nitrogen defect and boron dopant, Chem. Eng. J. 396 (2020) 125395.

[15] H. Hirakawa, M. Hashimoto, Y. Shiraishi, T. Hirai, Photocatalytic conversion of nitrogen to ammonia with water on surface oxygen vacancies of titanium dioxide, J. Am. Chem. Soc. 139 (2017) 10929-10936.

[16] H. Li, J. Shang, Z. Ai, L. Zhang, Efficient visible light nitrogen fixation with BiOBr nanosheets of oxygen vacancies on the exposed {001} facets, J. Am. Chem. Soc. 137 (2015) 6393-6399.

[17] Y. Bai, H. Bai, K. Qu, F. Wang, P. Guan, D. Xu, W. Fan, W. Shi, In-situ approach to fabricate BiOI photocathode with oxygen vacancies: understanding the N_2 reduced behavior in photoelectrochemical system, Chem. Eng. J. 362 (2019) 349-356.

[18] S. Wang, X. Hai, X. Ding, K. Chang, Y. Xiang, X. Meng, Z. Yang, H. Chen, J. Ye, Light-switchable oxygen vacancies in ultrafine Bi_5O_7Br nanotubes for boosting solar-driven nitrogen fixation in pure water, Adv. Mater. 29 (2017) 1701774.

[19] H. Guo, H.-Y. Niu, C. Liang, C.-G. Niu, D.-W. Huang, L. Zhang, N. Tang, Y. Yang, C.-Y. Feng, G.-M. Zeng, Insight into the energy band alignment of magnetically separable $Ag_2O/ZnFe_2O_4$ p-n heterostructure with rapid charge transfer assisted visible light photocatalysis, J. Catal. 370 (2019) 289-303.

[20] Y. Ma, X. Wang, Y. Jia, X. Chen, H. Han, C. Li, Titanium dioxide-based nanomaterials for photocatalytic fuel generations, Chem. Rev. 114 (2014) 9987-10043.

[21] G.N. Schrauzer, T.D. Guth, Photocatalytic reactions. 1. Photolysis of water and photoreduction of nitrogen on titanium dioxide, J. Am. Chem. Soc. 99 (1977) 7189-7193.

[22] Z. Wang, B. Wen, Q. Hao, L.M. Liu, C. Zhou, X. Mao, X. Lang, W.J. Yin, D. Dai, A. Selloni, X. Yang, Localized excitation of Ti^{3+} ions in the photoabsorption and photocatalytic activity of reduced rutile TiO_2, J. Am. Chem. Soc. 137 (2015) 9146-9152.

[23] K. Zhang, J.H. Park, Surface localization of defects in black TiO_2: enhancing photoactivity or reactivity, J. Phys. Chem. Lett. 8 (2017) 199-207.

[24] A. Al-Haddad, Z. Wang, R. Xu, H. Qi, R. Vellacheri, U. Kaiser, Y. Lei, Dimensional dependence of the optical absorption band edge of TiO_2 nanotube arrays beyond the quantum effect, J. Phys. Chem. C 119 (2015) 16331-16337.

[25] I.H. Öner, C.J. Querebillo, C. David, U. Gernert, C. Walter, M. Driess, S. Leimkühler, K.H. Ly, I.M. Weidinger, High electromagnetic field enhancement of TiO_2 nanotube electrodes, Angew. Chem. Int. Ed. 57 (2018) 7225-7229.

[26] G.L. Chiarello, A. Zuliani, D. Ceresoli, R. Martinazzo, E. Selli, Exploiting the photonic crystal properties of TiO_2 nanotube arrays to enhance photocatalytic hydrogen production, ACS Catal. 6 (2016) 1345-1353.

[27] N. Liu, V. Haublein, X. Zhou, U. Venkatesan, M. Hartmann, M. Mackovic, T. Nakajima, E. Spiecker, A. Osvet, L. Frey, P. Schmuki, "Black" TiO_2 nanotubes formed by high-energy proton implantation show noble-metal-co-catalyst free photocatalytic H_2-evolution, Nano Lett. 15 (2015) 6815-6820.

[28] I. Hanzu, T. Djenizian, P. Knauth, Electrical and point defect properties of TiO_2 nanotubes fabricated by electrochemical anodization, J. Phys. Chem. C 115 (2011) 5989-5996.

[29] X. Zhou, N. Liu, P. Schmuki, Photocatalysis with TiO_2 nanotubes: "colorful" reactivity and designing site-specific photocatalytic centers into TiO_2 nanotubes, ACS Catal. 7 (2017) 3210-3235.

[30] R.P. Lynch, A. Ghicov, P. Schmuki, A photo-electrochemical investigation of self-organized TiO_2 nanotubes, J. Electrochem. Soc. 157 (2010) G76-G84.

[31] X. Zhou, V. Haublein, N. Liu, N.T. Nguyen, E.M. Zolnhofer, H. Tsuchiya, M.S. Killian, K. Meyer, L. Frey, P. Schmuki, TiO_2 nanotubes: nitrogen-ion implantation at low dose provides noble-metal-free photocatalytic H_2-evolution activity, Angew. Chem. Int. Ed. 55 (2016) 3763-3767.

[32] F. Zhang, W. Pan, A missing step is a key step, Nat. Mater. 17 (2018) 851-852.

[33] Y. Ma, N. Wang, J. Chen, C. Chen, H. San, J. Chen, Z. Cheng, Betavoltaic enhancement using defect-engineered TiO_2 nanotube arrays through electrochemical reduction in organic electrolytes, ACS Appl. Mater. Interfaces 10 (2018) 22174-22181.

[34] E. Wahlstrom, E.K. Vestergaard, R. Schaub, A. Ronnau, M. Vestergaard, E. Laegsgaard, I. Stensgaard, F. Besenbacher, Electron transfer-induced dynamics of oxygen molecules on the TiO_2(110) surface, Science 303 (2004) 511-513.

[35] T. Close, G. Tulsyan, C.A. Diaz, S.J. Weinstein, C. Richter, Reversible oxygen scavenging at room temperature using electrochemically reduced titanium oxide nanotubes, Nat. Nanotechnol. 10 (2015) 418-422.

[36] N. Zhang, A. Jalil, D. Wu, S. Chen, Y. Liu, C. Gao, W. Ye, Z. Qi, H. Ju, C. Wang, X. Wu, L. Song, J. Zhu, Y. Xiong, Refining defect states in $W_{18}O_{49}$ by Mo doping: a strategy for tuning N_2 activation towards solar-driven nitrogen fixation, J. Am. Chem. Soc. 140 (2018) 9434-9443.

[37] G.W. Watt, J.D. Chrisp, Spectrophotometric method for determination of hydrazine, Anal. Chem. 24 (1952) 2006-2008.

[38] G. Kresse, J. Furthmüller, Efficient iterative schemes for ab initio total-energy calculations using a plane-wave basis set, Phys. Rev. B 54 (1996) 11169-11186.

[39] G. Kresse, D. Joubert, From ultrasoft pseudopotentials to the projector augmented-wave method, Phys. Rev. B 59 (1999) 1758-1775.

[40] P.E. Blöchl, Projector augmented-wave method, Phys. Rev. B 50 (1994) 17953-17979.

[41] J.P. Perdew, K. Burke, M. Ernzerhof, Generalized gradient approximation made simple, Phys. Rev. Lett. 77 (1996) 3865-3868.

[42] Y. Ji, Y. Luo, Theoretical study on the mechanism of photoreduction of CO_2 to CH_4 on the anatase TiO_2(101) surface, ACS Catal. 6 (2016) 2018-2025.

[43] N.S. Portillo-Vélez, O. Olvera-Neria, I. Hernández-Pérez, A. Rubio-Ponce, Localized electronic states induced by oxygen vacancies on anatase TiO_2 (101) surface, Surf. Sci. 616 (2013) 115-119.

[44] J. Zhang, Z. Yu, Z. Gao, H. Ge, S. Zhao, C. Chen, S. Chen, X. Tong, M. Wang, Z. Zheng, Y. Qin, Porous TiO_2 nanotubes with spatially separated platinum and CoO_x cocatalysts produced by atomic layer deposition for photocatalytic hydrogen production, Angew. Chem. Int. Ed. 56 (2017) 816-820.

[45] S. Wu, X. Tan, J. Lei, H. Chen, L. Wang, J. Zhang, Ga-doped and Pt-loaded porous TiO_2–SiO_2 for photocatalytic nonoxidative coupling of methane, J. Am. Chem. Soc. 141 (2019) 6592-6600.

[46] T. Xia, W. Zhang, J.B. Murowchick, G. Liu, X. Chen, A facile method to improve the photocatalytic and lithium-ion rechargeable battery performance of TiO_2 nanocrystals, Adv. Energy Mater. 3 (2013) 1516-1523.

[47] A. Sinhamahapatra, J.-P. Jeon, J.-S. Yu, A new approach to prepare highly active and stable black titania for visible light-assisted hydrogen production, Energy Environ. Sci. 8 (2015) 3539-3544.

[48] A. Chatzitakis, S. Sartori, Recent advances in the use of black TiO2 for production of hydrogen and other solar fuels, Chemphyschem 20 (2019) 1272-1281.

[49] Y. Zhang, Z. Ding, C.W. Foster, C.E. Banks, X. Qiu, X. Ji, Oxygen vacancies evoked blue TiO_2 (B) nanobelts with efficiency enhancement in sodium storage behaviors, Adv. Funct. Mater. 27 (2017) 1700856.

[50] Y. Yang, L.C. Yin, Y. Gong, P. Niu, J.Q. Wang, L. Gu, X. Chen, G. Liu, L. Wang, H.M. Cheng, An unusual strong visible-light absorption band in red anatase TiO_2 photocatalyst induced by atomic hydrogen-occupied oxygen vacancies, Adv. Mater. 30 (2018) 1704479.

[51] Y. Zhao, Y. Zhao, R. Shi, B. Wang, G.I.N. Waterhouse, L.-Z. Wu, C.-H. Tung, T. Zhang, Tuning oxygen vacancies in ultrathin TiO_2 nanosheets to boost photocatalytic nitrogen fixation up to 700 nm, Adv. Mater. 31 (2019) 1806482.

[52] Y. Chen, W. Li, J. Wang, Y. Gan, L. Liu, M. Ju, Microwave-assisted ionic liquid synthesis of Ti^{3+} self-doped TiO_2 hollow nanocrystals with enhanced visible-light photoactivity, Appl. Catal. B-Environ. 191 (2016) 94-105.

[53] W.-T. Kim, W.-Y. Choi, Fabrication of TiO_2 photonic crystal by anodic oxidation and their optical sensing properties, Sensor. Actuat A-Phys. 260 (2017) 178-184.

[54] X. Chen, L. Lei, P.Y. Yu, S.S. Mao, Increasing solar absorption for photocatalysis with black hydrogenated titanium dioxide nanocrystals, Science 331 (2011) 746-750.

[55] V.M. Khomenko, K. Langer, H. Rager, A. Fett, Electronic absorption by Ti^{3+} ions and electron delocalization in synthetic blue rutile, Phys. Chem. Miner. 25 (1998) 338-346.

[56] T.R. Gordon, M. Cargnello, T. Paik, F. Mangolini, R.T. Weber, P. Fornasiero, C.B. Murray, Nonaqueous synthesis of TiO_2 nanocrystals using TiF_4 to engineer morphology,

oxygen vacancy concentration, and photocatalytic activity, J. Am. Chem. Soc. 134 (2012) 6751-6761.

[57] T.W. Kim, Y. Ping, G.A. Galli, K.S. Choi, Simultaneous enhancements in photon absorption and charge transport of bismuth vanadate photoanodes for solar water splitting, Nat. Commun. 6 (2015) 8769.

[58] H. Seo, L.R. Baker, A. Hervier, J. Kim, J.L. Whitten, G.A. Somorjai, Generation of highly n-type titanium oxide using plasma fluorine insertion, Nano letter. 11 (2011) 751-756.

[59] N. D. Abazović, M. I. Čomor, M. D. Dramićanin, D. J. Jovanović, A. S Phillip, J. M. Nedeljković, Photoluminescence of anatase and rutile TiO_2 particles, J. Phys. Chem. B 110 (2006) 25366-25370.

[60] Q. Guo, C. Zhou, Z. Ma, X. Yang, Fundamentals of TiO_2 photocatalysis: concepts, mechanisms, and challenges, Adv. Mater. (2019) 1901997.

[61] G. Zhu, T. Lin, X. Lü, W. Zhao, C. Yang, Z. Wang, H. Yin, Z. Liu, F. Huang, J. Lin, Black brookite titania with high solar absorption and excellent photocatalytic performance, J. Mater. Chem. A 1 (2013) 9650-9653.

[62] Y. Sun, S. Gao, Y. Xie, Atomically-thick two-dimensional crystals: electronic structure regulation and energy device construction, Chem. Soc. Rev. 43 (2014) 530-546.

[63] K. Zhang, L. Wang, J.K. Kim, M. Ma, G. Veerappan, C.-L. Lee, K.-j. Kong, H. Lee, J.H. Park, An order/disorder/water junction system for highly efficient co-catalyst-free photocatalytic hydrogen generation, Energy Environ. Sci. 9 (2016) 499-503.

[64] A.J. Rettie, H.C. Lee, L.G. Marshall, J.F. Lin, C. Capan, J. Lindemuth, J.S. McCloy, J. Zhou, A.J. Bard, C.B. Mullins, Combined charge carrier transport and photoelectrochemical characterization of $BiVO_4$ single crystals: intrinsic behavior of a complex metal oxide, J. Am. Chem. Soc. 135 (2013) 11389-11396.

[65] L. Zhu, M. Gao, C.K.N. Peh, G.W. Ho, Solar-driven photothermal nanostructured materials designs and prerequisites for evaporation and catalysis applications, Mater. Horiz. 5 (2018) 323-343.

[66] Z. Hua, B. Li, L. Li, X. Yin, K. Chen, W. Wang, Designing a novel photothermal material of hierarchical microstructured copper phosphate for solar evaporation enhancement, J. Phys. Chem. C 121 (2016) 60-69.

[67] J. Wang, Y. Li, L. Deng, N. Wei, Y. Weng, S. Dong, D. Qi, J. Qiu, X. Chen, T. Wu, High-performance photothermal conversion of narrow-bandgap Ti_2O_3 nanoparticles, Adv. Mater. 29 (2017) 1603730.

[68] L. Liang, X. Li, Y. Sun, Y. Tan, X. Jiao, H. Ju, Z. Qi, J. Zhu, Y. Xie, Infrared light-driven CO_2 overall splitting at room temperature, Joule 2 (2018) 1004-1016.

[69] J. Deng, J.A. Iñiguez, C. Liu, Electrocatalytic nitrogen reduction at low temperature, Joule 2 (2018) 846-856.

[70] S. Liu, M. Wang, T. Qian, H. Ji, J. Liu, C. Yan, Facilitating nitrogen accessibility to boron-rich covalent organic frameworks via electrochemical excitation for efficient nitrogen fixation, Nat. Commun. 10 (2019) 3898.

[71] M. Nazemi, M.A. El-Sayed, Plasmon-enhanced photo(electro)chemical nitrogen fixation under ambient conditions using visible light responsive hybrid hollow Au-Ag_2O nanocages, Nano Energy 63 (2019) 103886.

[72] J.N. Kondo, S. Shibata, Y. Ebina, K. Domen, A. Tanaka, Preparation of a SiO_2-pillared $K_{0.8}Fe_{0.8}Ti_{1.2}O_4$ and IR study of N_2 adsorption, J. Phys. Chem. 99 (1995) 16043-16046.

[73] A. Zecchina, L. Marchese, S. Bordiga, C. Pazè, E. Gianotti, Vibrational spectroscopy of NH^{4+} ions in zeolitic materials: zn IR study, J. Phys. Chem. B 101 (1997) 10128-10135.

[74] M. Dunwell, Y. Yan, B. Xu, A surface-enhanced infrared absorption spectroscopic study of pH dependent water adsorption on Au, Surf. Sci. 650 (2016) 51-56.

[75] M.A. Légaré, G. Bélanger-Chabot, R.D. Dewhurst, E. Welz, I. Krummenacher, B. Engels, H. Braunschweig, Nitrogen fixation and reduction at boron, Science 359 (2018) 896-900.

[76] J. Zhao, Z. Chen, Single Mo atom supported on defective boron nitride monolayer as an efficient electrocatalyst for nitrogen fixation: a computational study, J. Am. Chem. Soc. 139 (2017) 12480-12487.

[77] C. Ling, X. Niu, Q. Li, A. Du, J. Wang, Metal-free single atom catalyst for N_2 fixation driven by visible light, J. Am. Chem. Soc. 140 (2018) 14161-14168.

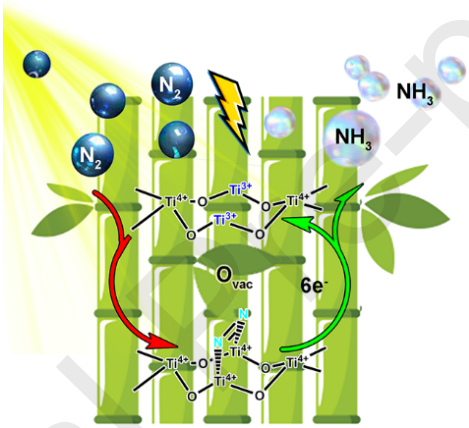

Highlights

- Defective TiO_2 nanobamboo arrays ($DTiO_2$ NBAs) are implanted on Ti foil by anodizing
- $DTiO_2$ NBAs adsorb UV-Vis-IR light (up to 780 nm) to activate N≡N bonds
- Highly selective NH_3 yield (48.3 mg m^{-2} h^{-1}) without sacrificial agent or noble-metal
- Alternating photo-fixation mechanism based on deconstructing N_2 adsorption on $DTiO_2$
- Rate-limiting step ($*NH_2 \rightarrow *NH_3$) with low energy barrier (0.37 eV) is conveyed by DFT

Declaration of interests

☒ The authors declare that they have no known competing financial interests or personal relationships that could have appeared to influence the work reported in this paper.